

# Measurement of Many-Body Quantum Correlations in Superconducting Circuits

Kamal Sharma\* and Wade DeGottardi†

*Department of Physics & Astronomy, Texas Tech University, Lubbock, TX*

(Dated: June 21, 2024)

Recent advances in superconducting circuit technology have made the fabrication of large, customizable circuits routine. This has led to their application to areas beyond quantum information and, in particular, to their use as quantum simulators. A key challenge in this effort has been the identification of the quantum states realized by these circuits. Here, we propose a probe circuit capable of reading out many-body correlations in an analog quantum simulator. Our measurement scheme, designed for many-photon states, exploits the non-linearity of the Josephson junction to measure two-point (and potentially higher-order) correlation functions of the superconducting phase operator. We demonstrate the capabilities of this design in the context of an LC-ladder with a quantum impurity. The proposed probe allows for the measurement of inherently quantum correlations, such as squeezing, and has the potential to significantly expand the scope of analog quantum simulations using superconducting circuits.

## I. INTRODUCTION

Superconducting circuits are macroscopic objects capable of exhibiting quantum behavior [1–3] and are the leading contenders to achieve large-scale quantum computation [4–6]. Dramatic advances in the technology associated with their fabrication, control, and measurement [7, 8] have made customized superconducting circuits widely available for a variety of applications outside of quantum computation. Of interest here is their use in realizing quantum many-body phenomena. Historically, discoveries in the field of many-body systems have required access to new materials and measurement techniques. Superconducting circuits are challenging this paradigm by allowing the creation of engineered quantum systems [9, 10]. Simulations of many-body systems using superconducting circuits fall into two broad classes: digital [11–13] and analog [14]. In digital simulations, the unitary dynamics of a target quantum system are calculated in discrete steps for a desired time interval. For example, digital simulations have been used to explore the one-dimensional Hubbard model [15] and quantum walks [16]. In analog simulations, the focus of interest here, the circuit couplings emulate a desired Hamiltonian, see e.g. [17]. Analog simulations have realized Mott insulating behavior [18], many-body localization [19], the superconductor–insulator transition [20], quantum impurities [19, 21], and hyperbolic lattices [22, 23]. Additionally, there have been numerous proposals to simulate photon pair condensates [24], hard-core bosons [25], Dicke chains [26], superfluids [27], and supersolids [28].

A key challenge in analog quantum simulations is identifying the many-body state realized. The measurement of traditional condensed matter systems typically involves probing the system in its ground state or thermal state by weak perturbations. From such measurements,

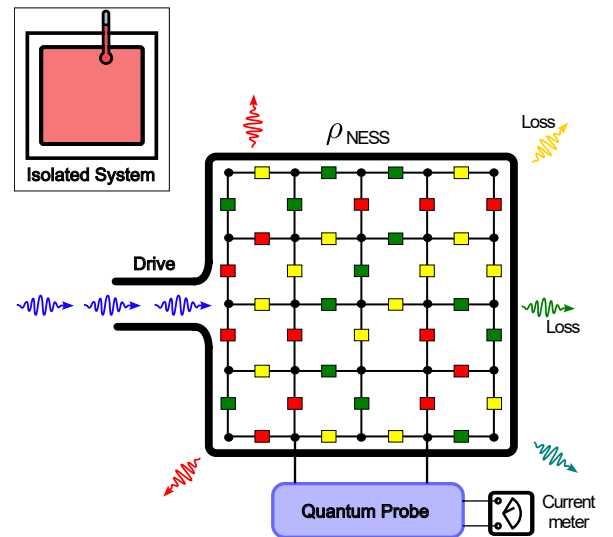


Figure 1. **Non-equilibrium steady-state.** A Superconducting circuit is composed of nodes (black dots) connected by one (or more) of three circuit elements (colored boxes): a capacitor, inductor, or Josephson junction. In general, the steady-state of the system takes a non-universal form and depends sensitively on the external drive, circuit parameters, and loss. On the other hand, the measurement of condensed matter systems (inset) typically involves weakly perturbing a thermal state.

correlation functions of various operators can be obtained using linear response theory and the fluctuation-dissipation theorem, in particular. In fact, the behavior of a many-body correlation function is often taken to define a quantum phase of matter. For example, the off-diagonal long-range order (ODLRO) of the many-body density matrix is a correlation function involving particle creation and annihilation operators at different points in space. The presence of ODLRO formally defines superfluidity [29].

However, unlike most condensed matter systems, superconducting circuits are lossy and typically probed far from equilibrium, as illustrated in Fig. 1. Hence, their

\* ksharma.phy@gmail.com

† wdegotta@ttu.edu

steady-state is neither the ground state nor a thermal state. Specially adapted measurement techniques are used to probe these circuits in non-equilibrium steady states (NESS). For example, reflectivity measurements are used to measure the spectra of circuits [18, 19, 21]. Other physical quantities measured experimentally include quadratures of the superconducting phase [30, 31] and photon populations [32]. However, the ability to measure many-body correlations, which is crucial to the identification of quantum phases, has not been demonstrated in superconducting circuit analog simulations.

The measurement of correlations is essential to detect certain quantum phenomena. While classical quantities always have well-defined values, quantum degrees of freedom often have intrinsic uncertainties. For an operator  $\hat{x}$  corresponding to a physical quantity, typically  $\langle \hat{x}^2 \rangle \neq \langle \hat{x} \rangle^2$  in general, where  $\langle \cdot \rangle$  denotes the quantum mechanical expectation value. This also occurs for two distinct physical quantities:  $\langle \hat{x}\hat{y} \rangle$  differs from  $\langle \hat{x} \rangle \langle \hat{y} \rangle$ , in general. Certain types of quantum order can only be detected through measurements involving the product of two operators, such as squeezing [33].

In this work, we demonstrate that for weakly coupled probes, the measurement of the product of two or more superconducting phase operators requires a Josephson junction. We propose a particular probe design, which is investigated in the context of an LC-ladder with a single quantum impurity. This setup bears many similarities with recent experiments in photonic cavities [19, 21] in that the quantum impurity gives rise to inelastic photon scattering. For example, a high energy photon can split into several lower energy ones. This process generates quantum correlations, such as single- and multi-state squeezing [33]. We consider several trial many-body wave functions incorporating the expected quantum correlations. We show that normal and anomalous correlation functions of the photon operators are encoded in Fourier components of the probe's output current. Detailed experimental estimates for the LC-ladder and the probe circuit are given, which are well within current experimental technology.

The outline of this paper is as follows. In Sec. II, we establish the general criteria that a many-body probe must satisfy. A particular probe design, tailored for the LC-ladder and quantum impurity system, is introduced in Sec. III. In Sec. IV, trial wave functions that capture the physics of the system are employed to demonstrate the probe's capabilities. Finally, Sec. V discusses our findings and future outlook.

## II. PROBE DESIGN

A superconducting circuit is defined by a set of nodes linked by an inductor, a capacitor, or a Josephson junction. The quantum dynamics of the system is captured by two operators describing the superconducting phase and the number of Cooper pairs on each node of the cir-

cuit. On the  $i^{\text{th}}$  node, these operators are denoted by  $\phi_i$  and  $n_i$ , respectively. These degrees of freedom are related to voltage and current and satisfy the canonical commutation relations described in Appendix B.

The primary goal of this paper is to introduce the design of a probe capable of measuring correlation functions involving two superconducting phases, such as  $\langle \phi_i \phi_j \rangle$ . The probe is also capable of measuring the expectation of a single superconducting phase operator,  $\langle \phi_i(t) \rangle$ . Here, we focus on the case in which the probe is weakly coupled to the system being measured. Rather than making projective measurements, the probe performs weak continuous measurements as it is driven by the system. A characteristic of weak measurements is that a signal is averaged over some period of time. We have identified three broad criteria that any such probe should satisfy:

1. *The probe should not significantly alter the dynamics of the system.* The probe should represent a small perturbation to the system so that its presence does not fundamentally alter the state of the system being measured. This is equivalent to the requirement that the impedance of the probe  $Z_P$  should be large compared with the characteristic impedance of the system  $Z_0$ . A related consideration is whether the system contains inductors. A system with only Josephson junctions and capacitors has a Hamiltonian that is periodic in its phases  $\phi_i$  [34]. In such cases, care must be taken not to include any inductors that could “pin” the phases of the system.
2. *In order to measure correlation functions involving two or more operators, the probe must contain a non-linear circuit element.* The measurement of quadratures  $\langle \phi_i \rangle$  and  $\langle n_i \rangle$  can be accomplished with linear circuits. However, the measurement of correlation functions involving more than one operator requires interaction terms in the circuit Hamiltonian (i.e, terms of cubic or quartic order). This follows from the form of Hamilton's equations of motion. A Josephson junction is thus necessary to obtain correlation functions of the form  $\langle \phi_i \phi_j \rangle$ . If a coherent non-linear circuit element involving the charge  $n_i$  could be devised, it would also be possible to measure the correlation functions  $\langle n_i n_j \rangle$ .
3. *The probe's output should be in the measurable range of current technology.* For example, the measurement of currents of the order of nanoamps is well within current experimental capabilities [35, 36].

An example of a probe that satisfies these criteria is shown in Fig. 2a. It is coupled to nodes  $i$  and  $j$  of the system. A feature of this particular design is that an external flux  $\varphi_{ext}$  tuned to either 0 or  $\pi/2$  selects whether the probe measures  $\langle \phi_i \rangle$  or two-operator correlation functions  $\langle \phi_i \phi_j \rangle$ , respectively. As shown in Fig. 2a, the probe

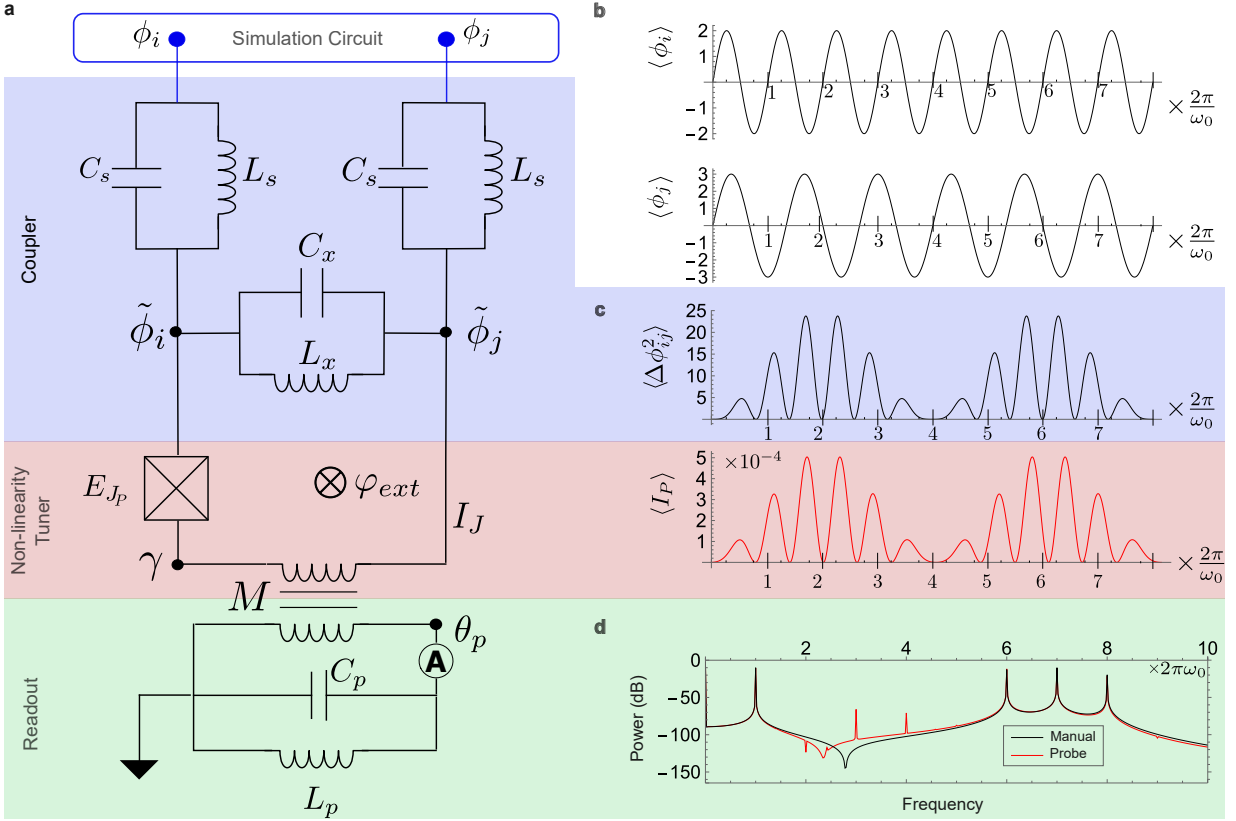


Figure 2. **Probe design and operation.** **a.** Proposed probe consists of three functional elements: a coupler, tuner, and readout. The output of the probe is encoded in the current in the readout circuit, which can be measured by an ammeter, indicated by **(A)**. **b.** Test signals for  $\langle \phi_i \rangle$  and  $\langle \phi_j \rangle$ , which are pure tones with frequencies  $4\omega_0$  and  $3\omega_0$ , respectively. **c.** Plot of  $\Delta\phi_{ij}^2$  (black) and simulated output current  $\langle I_P(t) \rangle$  (red) for  $\varphi_{ext} = \pi/2$ . **d.** Power spectral density of probe output current, showing dominant frequency components  $(3+3)\omega_0$ ,  $(4+4)\omega_0$ ,  $(4+3)\omega_0$ , and  $(4-3)\omega_0$ .

consists of three functional units: a coupler, a non-linear element tuned by the external flux, and a readout circuit. The probe's output is encoded in the current of the readout circuit.

The proposed probe behaves classically and its intrinsic quantum fluctuations are small compared to those of the input signal. This condition is satisfied for  $\omega_P \ll \omega_0$ , where  $\omega_P$  is the frequency of the readout circuit. This ensures that a single photon in the system corresponds to many quanta in the readout circuit, thus rendering it classical. For  $\Delta\phi_{ij} = \phi_i - \phi_j$ , the classical equation of motion gives a readout current

$$\langle I_P \rangle = \frac{\Phi_0 E_{J,P}}{2\pi L_P E_M} \sin(\beta \Delta\phi_{ij} + \varphi_{ext}), \quad (1)$$

where  $E_{J,P}$  is the energy associated with the Josephson junction in the non-linearity tuner,  $L_P$  is the inductance in the readout-out circuit, and  $E_M$  is the energy associated with the mutual inductance between the non-linearity tuner and the readout circuit (see Fig. 2). The parameter  $\beta$  is a function of the device parameters  $C_s, L_s, C_x$ , and  $L_x$ , see Appendix A for details. Our design requires that  $\beta \Delta\phi_{ij} \ll 1$ . Thus, selecting the appropriate circuit parameters requires a rough estimate of

the magnitude of the  $\phi_i$ 's in the circuit. As we will see, these values are ultimately set by the photon mode populations, which are controlled by the strength of the drive and the photon loss rates.

For  $\varphi_{ext} = 0$  and  $\beta \Delta\phi_{ij} \ll 1$ , Eq. (1) gives  $\langle I_P \rangle \propto \Delta\phi_{ij}$ . In this limit, the Josephson junction is equivalent to an inductor. By connecting one lead of the probe to node  $i$  and the other to ground, the probe's output yields  $\langle \phi_i \rangle$ . The true capabilities of the probe to measure correlations are achieved for  $\varphi_{ext} = \pi/2$ . For  $\beta \Delta\phi_{ij} \ll 1$ , we have  $\langle I_P \rangle \propto \cos \Delta\phi_{ij} \approx 1 - \beta^2 \langle \Delta\phi_{ij}^2 \rangle / 2$ . Then, we may obtain  $\langle \phi_i \phi_j \rangle$  by subtracting  $\langle \phi_i^2 \rangle$  and  $\langle \phi_j^2 \rangle$  from  $\langle \Delta\phi_{ij}^2 \rangle$ . The quantities  $\langle \phi_i^2 \rangle$  or  $\langle \phi_j^2 \rangle$  can be obtained by connecting one input of the probe to the  $i^{\text{th}}$  or  $j^{\text{th}}$  node of the circuit, and the other input to ground.

In Fig. 2**b-d**, the output of the probe for  $\varphi_{ext} = \pi/2$  has been simulated with the parameters provided in Appendix A based on a sample/test input for  $\langle \phi_i \rangle$  and  $\langle \phi_j \rangle$ . The input is classical and  $\phi_i$  and  $\phi_j$  are single tones, as shown in Fig. 2**b**. As shown in Fig. 2**c**, the probe's output matches the expectations outlined in the previous paragraph. The power spectrum shown in Fig. 2**d** illustrates that the signal is dominated by  $\Delta\phi_{ij}^2$ . Additional

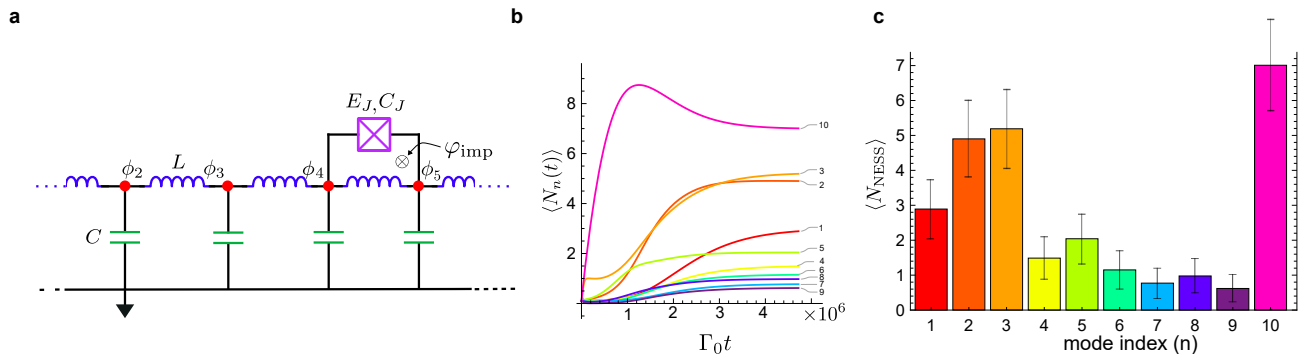


Figure 3. **System dynamics.** **a.** Superconducting analog simulator consists of an LC-ladder with a Josephson junction across nodes  $\{i_0, j_0\} \equiv \{4, 5\}$ , which acts as a quantum impurity. The magnetic flux  $\varphi_{\text{imp}}$  is set to  $\pi/2$  to generate a cubic coupling between mode pairs. **b.** Time evolution of the expected photon number for the lowest frequency modes of the circuit. The tenth mode, which is resonant with the external drive, overshoots its eventual steady-state value. **c.** Expectation values of photon number in the steady-state. The error bars depict the quantum fluctuations in the photon population of modes for the trial wavefunction  $\Psi_C$ .

weaker peaks in the range  $(2-4)\omega_0$  correspond to higher order terms in the expansion of the cosine. This simulation accounts for the finite lifetime of the photons in the probe (taken to be  $\kappa$ , the same lifetime as photons in the system, see Appendix A for details). In the limit  $\kappa \rightarrow 0$ , the peaks would become delta functions. In an actual circuit, the input signal is quantum rather than classical. The magnitude and nature of the quantum fluctuations depend on the system being measured, and we thus defer a discussion of these effects until Sec. IV.

In addition to the general criteria enumerated above, there are a number of additional design guidelines for the probe design. For example, the resonance frequency of the coupler, given approximately by  $\omega_x = 1/\sqrt{C_x L_x}$ , should not lie within the bandwidth of the system being measured as this would disproportionately amplify those elements of the signal near  $\omega_x$ . Other design considerations and characteristic circuit parameters are given in Appendix A.

### III. PHOTON CAVITY WITH A QUANTUM IMPURITY

In order to explore the capabilities of the probe described in Sec. II, we consider an analog simulator consisting of an LC-ladder with a quantum impurity. The ladder, shown in Fig. 3a, is taken to have  $N \gg 1$  circuit nodes. Since  $N$  is large, the low energy dispersion is linear,  $\omega_n = n\omega_0$ , where  $\omega_0 = \pi/(N+1)(LC)^{1/2}$ . The Hamiltonian of the ladder is  $H_0 = \sum_n \hbar\omega_n a_n^\dagger a_n$ . Here,  $a_n$  ( $a_n^\dagger$ ) is the photon annihilation (creation) operator for the  $n^{\text{th}}$  mode. The superconducting phase, expressed in terms of these mode operators, is

$$\phi_i = \sum_n \gamma_n(i) (a_n^\dagger + a_n), \quad (2)$$

where  $\gamma_n(i)$  is essentially the spatial wave function for the  $n^{\text{th}}$  mode on the  $i^{\text{th}}$  site (see Appendix B 1).

A flux-biased Josephson junction, which couples sites  $i_0$  and  $j_0$  of the ladder, plays the role of the quantum impurity. The impurity Hamiltonian, derived in Appendix B 1), is given by

$$H_{\text{imp}} = g \sum_{nml} A_{nml} a_n^\dagger a_m^\dagger a_l + h.c., \quad (3)$$

where  $g = E_J(E_C/E_L)^{3/4}$  sets of the overall energy scale and the  $A_{nml}$  are  $\mathcal{O}(1)$  dimensionless constants. The full Hamiltonian of the system is  $\mathcal{H} = H_0 + H_{\text{imp}} + H_{\text{drive}}$ , where  $H_{\text{drive}}$  corresponds to the external drive used to excite the system. The effects of photon loss are described by a quantum Liouville operator  $\mathcal{L}$ . The time-dependence of the many-body density matrix  $\rho$  is given by

$$\frac{\partial \rho}{\partial t} = -i[\mathcal{H}, \rho] + \mathcal{L}[\rho], \quad (4)$$

where the quantum Liouville operator  $\mathcal{L}$  is given in Appendix C.

We give a qualitative description of the dynamics described by Eq. (4). Starting from a system in its ground state, an external drive resonant with one of the ladder modes is turned on. As the driven mode is populated, scattering from the impurity gives rise to inelastic photon scattering, which begins populating the other modes. As the modes are populated, photon loss increases. Eventually, a steady-state is achieved. This physical picture of the system dynamics is confirmed by a simulation of the time-dependent photon population. The results are shown in Figure 3b. This simulation employs a master equation approach based on the dynamics of Eq. (4). This calculation, which assumes Fermi's golden rule, gives the correct dynamics for times  $t \gg 1/g$ . However, Fermi's golden rule is inapplicable for  $t \lesssim 1/g$ . This explains the lack of coherent effects, such as Rabi oscillations, in our simulation. It is worth noting that in Ref. [19], the system is in a many-body localized regime.

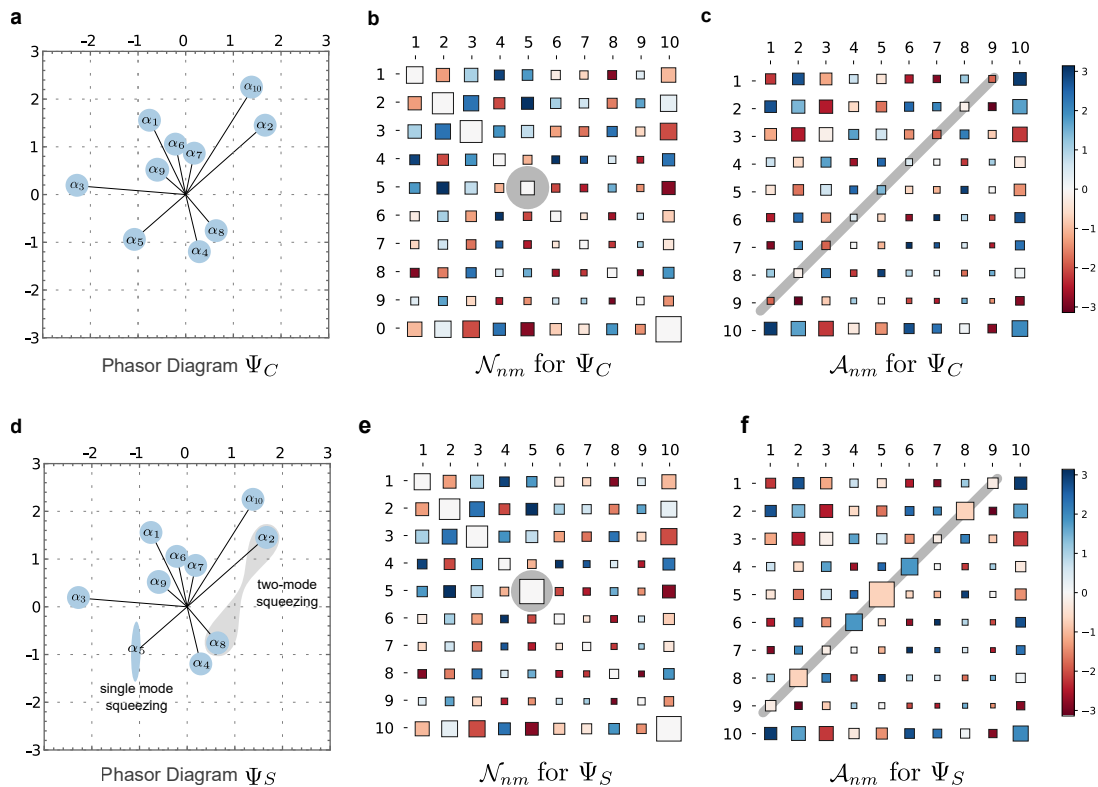


Figure 4. **Many-body correlations.** **a**, Phasor diagram for the trial wave function  $\Psi_C$  showing the magnitude and phase of the coherent state parameters  $\alpha_n$ . **b**, Hinton plot of  $\mathcal{N}_{nm}$  for  $\Psi_C$ , where the area of each box indicates the magnitude and the color indicates the phase. **c**, Hinton plot of  $\mathcal{A}_{nm}$  for  $\Psi_C$ . **d**, Phasor diagram for the trial wave function  $\Psi_S$  illustrating both single-mode and two-mode squeezing. Correlations  $\mathcal{N}_{nm}$  (**d**) and  $\mathcal{A}_{nm}$  (**e**) for  $\Psi_S$ . Highlighted boxes (gray) indicate differences between in  $\mathcal{N}_{nm}$  and  $\mathcal{A}_{nm}$  for  $\Psi_C$  and  $\Psi_S$ .

In that experiment, the long-time limit in which Fermi's golden rule would hold is inaccessible due to photon loss.

#### IV. MANY-BODY CORRELATIONS

The simulation of the photon population presented in the previous section provides the photon population of the steady-state density matrix, which is given by  $\text{Tr}(\rho a_i^\dagger a_i)$  (see Fig. 3c). The many-body correlation functions of interest here involve off-diagonal elements of the density matrix, analogous to ODLRO. Even for the modestly-sized system studied here, a full numerical calculation of the steady-state density matrix is impractical. That said, the physics of photon down-conversion has been well-studied in small systems and, in certain limits, exact solvable models are obtained [37]. As described below, one of the features exhibited by these systems is squeezing. We thus consider a number of trial wave functions that capture these features and match the steady-state photon population shown in Fig. 3c.

The trial wave functions we consider are based on the product state  $\Psi_C = |\alpha_1\rangle \otimes |\alpha_2\rangle \dots \otimes |\alpha_{10}\rangle$ , where  $|\alpha_i\rangle$  is a single-mode coherent state, see Appendix D. Although  $\Psi_C$  itself is essentially classical [33], it serves as

a useful benchmark for more realistic trial wave functions considered below. As we argue here, the parameters  $\alpha_i$  are readily measured by setting the probe's control flux  $\varphi_{ext}$  to zero, which allows a measurement of  $\langle \phi_i \rangle$ , for example. According to Eq. (2), this quantity is composed of Fourier modes  $\gamma_n(i) \mathcal{Q}_n(t)$ , where  $\mathcal{Q}_n(t) = \langle a_n^\dagger + a_n \rangle = \alpha_n e^{-i\omega_n t} + \alpha_n^* e^{i\omega_n t}$ . The  $\mathcal{Q}_n(t)$  can be obtained for all  $n$  from a single measurement of  $\langle \phi_i \rangle$  by decomposing the signal into its Fourier components. This assumes that the wave functions  $\gamma_n(i)$  are known. In Fig. 4a, a phasor plot of  $\Psi_C$  is given. The magnitudes of the  $\alpha_n$  have been selected to match the NESS photon number population found from the solution of the master equation. The phases of the  $\alpha_i$  have been assigned at random. In an actual experiment, these phases contain information about the history of the system before reaching the steady-state. It is important to note that the quantum fluctuations associated with the coherent state place a fundamental limit on the probe's ability to measure the magnitudes and phases of the  $\mathcal{Q}_n(t)$ . The magnitude of these quantum fluctuations are shown as error bars in Fig. 3c.

We now introduce a wave function that accounts for non-classical effects, such as squeezing. The wave function  $\Psi_S$  is obtained by applying the two-mode squeezing

operators  $S(\xi_{nm}) = \exp(\xi_{nm}^* a_n a_m - \xi_{nm} a_n^\dagger a_m^\dagger)$  to  $\Psi_C$  (see Appendix D3 for the full form). Squeezing arises from the interaction (3) mediated by the quantum impurity. In fact, the propagator  $\exp(-iH_{\text{imp}}\Delta t/\hbar)$  takes the form of  $S(\xi_{nm})$  in the limit that the driven mode (mode 10) is a coherent state such that  $a_{10} \rightarrow \alpha_{10}e^{-i\omega_{10}t}$ . Matching these two expressions gives a squeezing parameter  $\xi_{nm} = i\alpha_{10}e^{-i\omega_{10}t}gA_{nm,10}t/\hbar$ . Here, we consider the limit in which the effects of squeezing by the tenth mode dominate, and thus we do not include the effects of other modes.

Since  $|\xi_{nm}| \propto t$ , ostensibly the squeezing parameter will grow without bound. In fact, an exact solution of a two-mode model shows that this does occur in a strong pumping regime [37]. However, the regime of interest here falls within the weak pumping regime in which the magnitude of the squeezing parameter reaches a steady-state value. Based on the exact solution [37], we take  $\xi_{nm} = i\alpha_{10}e^{-i\omega_{10}t}A_{nm,10}T_*/\hbar$ , where  $T_*$  is a phenomenological parameter of the order of the time it takes the system to reach the steady-state.

Detecting squeezing requires measuring two-body correlation functions—the values of  $\mathcal{Q}_n(t)$  are identical for  $\Psi_C$  and  $\Psi_S$ . As described in Sec. II, for the control flux  $\varphi_{\text{ext}} = \pi/2$ , the probe can measure  $\langle\phi_i^2\rangle$  and  $\langle\phi_i\phi_j\rangle$ . Applying the mode expansion (2), we can express these expectations in terms of the normal and anomalous photon correlation functions given by

$$\mathcal{N}_{nm}(t) = \langle a_n^\dagger a_m + a_m^\dagger a_n \rangle / 2, \quad (5a)$$

$$\mathcal{A}_{nm}(t) = \langle a_n^\dagger a_m^\dagger + a_m a_n \rangle / 2, \quad (5b)$$

respectively. In the weak impurity regime considered here, the quantities  $\mathcal{N}_{nm}$  and  $\mathcal{A}_{nm}$  consist of a single frequency. In Fig. 4, the magnitude and phase of these quantities is plotted for the trial wave functions  $\Psi_C$  and  $\Psi_S$ . The effects of two-mode squeezing are apparent if we compare the diagonal values  $\mathcal{A}_{n,10-n}$  for the  $\Psi_C$  and  $\Psi_S$  (cf. Figs. 4 **c** and **f**). Additionally, the interaction (3) generates intra-mode squeezing for  $n = 5$ , which leads to an enhancement of  $\mathcal{N}_{5,5}$  (cf. Figs. 4 **b** and **e**). A measure of the strength of squeezing is given by

$$\mathcal{S}_{nm} = \mathcal{N}_{nm} + \mathcal{A}_{nm} - 2\mathcal{Q}_n\mathcal{Q}_m. \quad (6)$$

This quantity vanishes for  $\Psi_C$  or any state whose correlation functions obey clustering, i.e.,  $\langle\phi_i\phi_j\rangle = \langle\phi_i\rangle\langle\phi_j\rangle$ . It is non-zero for  $\Psi_S$ . Hence,  $\mathcal{S}_{nm}$  quantifies the strength of non-classical correlation between the  $n$  and  $m$  modes.

An important measure of the probe's effectiveness is the number of distinct measurements  $\langle\phi_i\rangle$  or  $\langle\phi_i\phi_j\rangle$  that are required to obtain all the correlations  $\mathcal{Q}_n$ ,  $\mathcal{N}_{nm}$ , and  $\mathcal{A}_{nm}$ . Provided that the wave functions  $\gamma_n(i)$  are known, for the weakly coupled LC-ladder all  $\mathcal{Q}_n$  can be obtained from  $\langle\phi_i\rangle$  for a single site  $i$ . As discussed above, this follows from the fact that each  $\mathcal{Q}_n$  corresponds to a distinct frequency. In turn, this follows from the non-degenerate spectrum of  $H_0$ . In principle, the many-body correlations  $\mathcal{N}_{nm}$  and  $\mathcal{A}_{nm}$  could be obtained from  $\langle\phi_i\phi_j\rangle$  for

a single pair of sites  $i$  and  $j$ . However, the harmonic spectrum exhibited by  $H_0$  gives rise to correlation functions that are degenerate in frequency. For example, both  $\mathcal{A}_{34}$  and  $\mathcal{A}_{52}$  are degenerate with a frequency of  $7\omega_0$ . In such cases, the required number of measurements will be equal to the largest degeneracy. As long as each measurement is linearly independent from the others, the number of equations matches the number of unknowns, so all the correlation functions can be obtained. For the linear spectrum considered here, the largest degeneracy for either  $\mathcal{N}_{nm}$  and  $\mathcal{A}_{nm}$  goes as  $\mathcal{O}(N)$ , and thus  $\mathcal{O}(N)$  independent measurements of  $\langle\phi_i\phi_j\rangle$  are required. Thus, the equally-spaced spectrum represents a worst-case scenario in terms of the number of measurements required since the number of degeneracies is large. In the NESS state considered in this paper, only three of the photon modes were appreciably populated. In such cases, only a few measurements are needed to capture the dominant behavior of the correlation functions.

## V. SUMMARY AND OUTLOOK

In this work, we have proposed a probe circuit capable of measuring quantum correlations in analog quantum simulators built from superconducting circuits. This probe can detect the effects of squeezing, an inherently quantum mechanical effect. The capabilities of the probe were explored in a particularly simple system: an LC-ladder with a quantum impurity. This system shares many similarities with recent experiments involving a quantum impurity in a photonic cavity [19, 21]. The ability to measure correlation functions has been a boon to quantum simulators based on cold atoms [38–40]. The proposed probe offers similar capabilities that would significantly expand the power of superconducting circuits based simulators.

To make the analysis tractable, we focused on a weakly coupled system. However, the proposed probe will be particularly important in strongly coupled systems, for which there is no good theoretical understanding. In such cases, the measurement of  $\langle\phi_i(t)\rangle$  would reveal the energy and nature of long-lived quasiparticles. The measurement of quantum correlations is crucial for distinguishing various types of quantum order. The proposals for analog quantum simulations include a broad spectrum of physical systems, including the sine-Gordon model [41], photon condensates [24], the Mott insulator to superfluid transition [27], as well as supersolids [28]. Given the importance of correlations in identifying and distinguishing quantum phases, the probe considered here has the potential to enhance the scope of analog quantum simulations.

## ACKNOWLEDGMENTS

We thank Mohammad Hafezi and Brian Kennedy for their insightful comments.

## Appendix A: Probe Parameters

The probe couples to nodes  $i$  and  $j$  of the system to be measured, as shown in Fig. 2a of the main text. The equations of motion for the probe degrees of freedom state that the probe responds to the superconducting flux difference  $\Delta\phi_{ij} \equiv \phi_i - \phi_j$ . Here, we focus on the readout signal arising from at  $n^{\text{th}}$  Fourier mode, i.e.,  $\Delta\phi_{ij} = A_n e^{i\omega_n t}$ , of the input signal  $\Delta\phi_{ij}$ . The purpose of the coupler stage (shown in blue in Fig. 2a) is to scale the incoming signal so that the Josephson junction operates in the nearly linear regime. We denote this scale factor  $\beta$ , i.e., with  $\Delta\tilde{\phi}_{ij} \equiv \beta\Delta\phi_{ij}$ , where  $\Delta\tilde{\phi}_{ij} = \tilde{\phi}_i - \tilde{\phi}_j$ . The quantities  $\tilde{\phi}_{i,j}$  are defined in Fig. 2. The classical equations of motion give

$$\beta = \frac{1/L_S - C_S\omega^2}{(1/L_S + 2/L_X) - (C_S + 2C_X)\omega^2}, \quad (\text{A1})$$

where we have used the fact that the impedance drop across the non-linearity tuner is much larger than that of the coupler. The parameter  $\beta$  is selected so that  $\beta\Delta\phi_{ij} \ll 1$ , but the non-linear part of the Josephson junctions current is still measurable. The particular value of  $\beta$  will depend on the photon population of the steady-state, which controls  $\Delta\phi_{ij}$ .

The quantity  $\Delta\tilde{\phi}_{ij}$  becomes the input for the non-linearity tuner. Provided that the impedance drop across the Josephson junction greatly exceeds that across the inductor  $M$ , then  $\gamma \approx \phi_j$  and the current through the Josephson junction is

$$I_J = I_c \sin(\Delta\tilde{\phi}_{ij} + \varphi_{ext}) \quad (\text{A2})$$

The external flux  $\varphi_{ext}$  controls the correlation function that is to be measured. The final stage of the probe is the read-out circuit (green), which is designed to generate a current that is proportional to  $I_J$ . In fact, one of the classical equations of motion for the circuit is  $\theta_p = (E_{JP}I_J/E_M I_C)$  which, together with Eq. (A2), gives Eq. (1) of the main text.

In Table I, we give characteristic parameters of the system, and Tables II and III provide estimates for the probe parameters. These values satisfy the sundry conditions laid out in the text and in this Appendix and are well within reach of current experimental technology, see e.g. [19].

## Appendix B: System Description

We consider a superconducting circuit design for simulating a photonic cavity with a weak non-linear quantum impurity. The impurity induces cubic coupling between the cavity modes quantified by  $g$ . We design our circuit parameters such that  $g \ll \omega_0$ , where  $\omega_0$  is the frequency of the lowest energy cavity mode. Additionally, the photon loss rate  $\kappa$  is much less than the rate of downconversion which can be calculated using Fermi's golden rule.

System Parameters	Value
$N$	51
$L_0$	254 pH
$C_0$	100 fF
$\omega_0$	16 MHz
$E_J/h$	3 GHz
$g/h$	5 MHz
$Z_0$	50 $\Omega$
$\Omega_0$	18 kHz
$\kappa$	1.2 kHz

Table I. System parameters.

Probe Parameters	Value
$C_S$	10 fF
$L_S$	100 $\mu\text{H}$
$C_X$	10 fF
$L_X$	100 $\mu\text{H}$
$E_{JP}/h$	3 GHz
$I_{JPc}$	1 nA
$M$	10 nH
$C_P$	10 nH

Table II. Probe parameters

This ensures that the photons undergo many downconversion events before escaping the system.

### 1. Superconducting cavity

The photonic cavity is modeled by a ladder circuit of inductors and capacitors, as shown in Fig. 3a of the text. As is customary for superconducting circuits, we begin by writing down the Lagrangian of the circuit. For the ladder, we have

$$\mathcal{L}_0(\Phi_i, \dot{\Phi}_i) = \sum_{j=1}^N \frac{C\dot{\Phi}_j^2}{2} - \sum_{j=0}^N \frac{(\Phi_{j+1} - \Phi_j)^2}{2L}, \quad (\text{B1})$$

where,  $\Phi_i = \int_{-\infty}^t V_i(\tau) d\tau$  is the node flux. To obtain the Hamiltonian, we use the fact that the conjugate momentum to  $\Phi_i$  is  $\partial\mathcal{L}_0/\partial\dot{\Phi}_i = C\dot{\Phi}_i$ , which we identify as the charge  $Q_i$  associated with the node. The Legendre transformation of the Lagrangian  $\sum_i \Phi_i Q_i - \mathcal{L}_0$  results

Probe Parameters	Value
$Z_P$	126 $\Omega$
$\omega_P$	50 MHz
$\beta$	0.3
$I_{P,critical}$	20 pA

Table III. Probe parameters.

in the Hamiltonian  $H_0$

$$H_0(\Phi_i, Q_i) = \sum_{j=0}^N \frac{Q_j^2}{2C} + \sum_{j=0}^N \frac{(\Phi_{j+1} - \Phi_j)^2}{2L} \quad (\text{B2})$$

It is convenient to write the charge and flux operators as  $Q_j = 2en_j$  and flux operators  $\Phi_j = \frac{\Phi_0}{2\pi} \phi_j$ .

$$H_0 = \sum_{j=1}^N 4E_C n_j^2 + \frac{1}{2} \sum_{j=0}^N E_L (\phi_{j+1} - \phi_j)^2, \quad (\text{B3})$$

where  $E_C = \frac{4e^2}{2C}$  and  $E_L = \left(\frac{\Phi_0}{2\pi}\right)^2 \frac{1}{2L}$ . The dimensionless operators  $n_j$  and  $\phi_k$  obey the canonical commutation relations  $[n_j, \phi_k] = i\delta_{jk}$ , which follow from the definitions above.

We take the LC ladder to be terminated at its ends so that  $\phi_0 = \phi_{N+1} = 0$ . The classical solution of the flux obeying these boundary conditions is given by the normal modes and the allowed normal mode frequencies

$$X_n(i) = \sqrt{\frac{2}{N+1}} \sin\left(\frac{n\pi i}{N+1}\right), \quad (\text{B4})$$

$$\omega_n = \frac{2}{\sqrt{LC}} \sin\left(\frac{n\pi}{2N+2}\right), \quad (\text{B5})$$

where,  $X_n(i)$  is the spatial profile of the  $n^{\text{th}}$  mode at node  $i$ . These eigenmodes satisfy the orthogonality relations

$$\sum_i X_n(i) X_m(i) = \delta_{nm}. \quad (\text{B6})$$

We introduce the photon creation  $a_n^\dagger$  and annihilation ( $a_n$ ) operators as

$$\phi_m = \phi_m^{zpf} (a_m + a_m^\dagger), \quad (\text{B7})$$

$$n_m = -in_m^{zpf} (a_m - a_m^\dagger). \quad (\text{B8})$$

The coefficients

$$\phi^{zpf} = \sqrt{\frac{N+1}{m\pi}} \left(\frac{2E_C}{E_L}\right)^{1/4}, \quad (\text{B9})$$

$$n^{zpf} = \sqrt{\frac{m\pi}{N+1}} \left(\frac{E_L}{32E_C}\right)^{1/4} \quad (\text{B10})$$

quantify the magnitude of the zero point fluctuations of flux and charge, respectively. For simplicity, we combine the zero point fluctuation  $\phi^{zpf}$  and the spatial mode  $X_n(i)$  into one variable

$$\gamma_n(i) = \phi_n^{zpf} X_n(i). \quad (\text{B11})$$

This allows us to write the Hamiltonian B3 as

$$H_0 = \sum_n \hbar m \omega_0 \left( a_n^\dagger a_n + \frac{1}{2} \right), \quad (\text{B12})$$

where, for large circuits,  $N \gg 1$ , the low-lying modes are roughly equally spaced in frequency  $\omega_n = n\omega_0$ , with

$$\omega_0 = \frac{\pi}{N+1} (LC)^{-1/2}. \quad (\text{B13})$$

## 2. Josephson junction impurity

The Hamiltonian of the Josephson junction impurity shown in Fig. 3a is

$$H_{\text{imp}} = -E_{J,\text{imp}} \cos(\phi_{i_0} - \phi_{j_0} + \varphi_{\text{imp}}), \quad (\text{B14})$$

where  $E_{J,\text{imp}}$  is the Josephson energy and the junction is connected between the nodes  $i_0$  and  $j_0$  of the LC-ladder. The tunable magnetic flux  $\varphi_{\text{imp}}$  changes the functional form of the non-linearity. When  $\varphi_{\text{imp}} = \pi/2$ , the leading terms in the expansion of  $H_{\text{imp}}$  gives the linear and cubic contributions

$$H_{\text{imp}} \approx E_{J,\text{imp}} \left[ (\phi_{i_0} - \phi_{j_0}) - \frac{(\phi_{i_0} - \phi_{j_0})^3}{3!} \right]. \quad (\text{B15})$$

Any odd power, in  $\phi$ , perturbation to the harmonic Hamiltonian vanishes to first order in perturbation theory. However, the cubic term in equation B15 induces the downconversion of photons even in the first order. In terms of the creation and annihilation operators B8, the impurity Hamiltonian is given by

$$H_{\text{imp}} = g \sum_{nml} A_{nml} (a_n^\dagger a_m^\dagger a_l + h.c.) \quad (\text{B16})$$

where the energy scale of the coupling,

$$g = E_J \left(\frac{E_C}{E_L}\right)^{3/4},$$

appearing in Eq. (3) is determined by the energies  $E_J, E_C$ , and  $E_L$ . The dimensionless coupling matrix  $A_{nml} \equiv A_{nml}(i_0, j_0)$  explicitly expressed as

$$A_{nml}(i_0, j_0) = \left(\sqrt{2/\pi}\right)^3 2^3 2^{3/4} f_n f_m f_l, \quad (\text{B17})$$

where,

$$f_n = \frac{1}{\sqrt{n}} \sin \frac{n\pi(i_0 - j_0)}{2N+1} \cos \frac{n\pi(i_0 + j_0)}{2N+1}$$

depends on the set of nodes  $\{i_0, j_0\}$  connected to the Josephson junction and determines the strength of coupling among the modes  $n, m, l$ . The rotating-wave approximation has been applied in deriving  $H_{\text{imp}}$  and so only energy conserving terms satisfying  $n\omega_0 + m\omega_0 = l\omega_0$  appear in the Hamiltonian (3).

## Appendix C: Mode population dynamics

The time evolution of the photon population  $\langle N_n \rangle$  for each mode  $n$  can be calculated by solving the master equation for the diagonal elements of  $\rho$ . For any given mode  $n$ , the photon down-conversion process leads to a cascade of photons filling up and leaving the single-particle state corresponding to the mode  $n$ . For weak

coupling between the modes, the rate of this process is determined by Fermi's golden rule

$$\Gamma_{down} = \Gamma \sum_{ml} A_{nml}^2 [(N_n + 1)(N_m + 1)N_l - N_n N_m (N_l + 1)] \delta_{l, n+m} \quad (C1)$$

where  $\Gamma \sim E_J^2 / (\hbar^2 \omega_0)$ . Downconversion continues from the newly populated states to more low-energy pairs, resulting in four photons. This continues till a steady state is reached.

The inevitable coupling of our system with the environment causes the photons to be lost from the circuit at a rate,  $\kappa$ . To account for photon loss, we work in the Markovian approximation. Additionally, we assume that the environment around our system is at  $T = 0$  K. Therefore, no photons are scattered back from the environment into the system. Thus, the rate of photon loss from a given mode is proportional to the photon population of that state. In this case, the Liouville operator in Eq. (4) simplifies to

$$\mathcal{L}[\rho] = -\kappa \sum_m n_m |n_m\rangle \langle n_m|. \quad (C2)$$

These two contributions are used to solve for the  $N_n$  as a function of time. The master equation, thus, leads to a set of coupled differential equations for the mode population which can be solved numerically.

$$\dot{N}_n = \Gamma_{down} + \Omega_{drive} - \kappa N_n, \quad (C3)$$

where  $\Omega_{drive} = \Omega_0 e^{-i\omega_{10}t}$ . The effective strength  $\Omega_0$  of the driving tone is a function of the drive parameters and its coupling with the LC-ladder.

#### Appendix D: Trial wavefunctions

Here, we consider four trial wavefunctions that exemplify some of the many-body physics exhibited by large superconducting circuits.

##### 1. Coherent states

Coherent states  $|\alpha\rangle$  of a harmonic oscillator  $H = \hbar\omega(a^\dagger a + 1/2)$  are the eigenstates of the lowering operator  $a$ . Another way to define coherent states is that they are the displaced vacuum state  $|\alpha\rangle = D(\alpha)|0\rangle$ , where

$$D(\alpha) = e^{\alpha a^\dagger - \alpha^* a}, \quad (D1)$$

is the displacement operator. By extension, correlation functions for a product coherent state for a system of  $N$  harmonic oscillators

$$|\Psi_C\rangle = \prod_{n=1}^N D_n(\alpha_n)|0\rangle \quad (D2)$$

are derived using

$$D^\dagger(\alpha) a D(\alpha) = a + \alpha \quad (D3)$$

$$D^\dagger(\alpha) a^\dagger D(\alpha) = a^\dagger + \alpha^*. \quad (D4)$$

The quadratures for  $\Psi_C$  obtained from Eqs. 5 are

$$\mathcal{Q}_n(t) = \frac{1}{2} (\alpha_n e^{-i\omega_n t} + \alpha_n^* e^{i\omega_n t}), \quad (D5)$$

while the correlation functions have the form

$$\mathcal{N}_{nm}(t) = \frac{1}{2} (\alpha_n^* \alpha_m e^{-i(\omega_m - \omega_n)t} + c.c.), \quad (D6)$$

$$\mathcal{A}_{nm}(t) = \frac{1}{2} (\alpha_n^* \alpha_m^* e^{i(\omega_m + \omega_n)t} + c.c.). \quad (D7)$$

We see that the correlation functions obey the relation

$$\mathcal{N}_{nm} + \mathcal{A}_{nm} - 2\mathcal{Q}_n \mathcal{Q}_m = 0, \quad (D8)$$

which reflects clustering of the correlation functions.

## 2. Fock States

The state  $|\Psi_N\rangle$  is defined to be a product of the number eigenstates for the various modes,

$$|\Psi_N\rangle = \prod_{m=1} \frac{1}{\sqrt{N_m!}} (a_m^\dagger)^{N_m} |0\rangle. \quad (D9)$$

where  $N_m$  is the number of photons in mode  $m$ . In this case, we find

$$\mathcal{Q}_n = 0, \quad (D10)$$

$$\mathcal{N}_{nm} = N_m \delta_{nm}, \quad (D11)$$

$$\mathcal{A}_{nm} = 0. \quad (D12)$$

## 3. Multi-Mode Squeezed State

We consider a trial wavefunction  $\Psi_S$  that exhibits two-mode squeezing, with each mode appearing in exactly one squeezing operator. This state is specified by partitioning the mode numbers into sets of two—membership in the same set indicates that these pair of modes are being simultaneously squeezed. This state can be written

$$|\Psi_S\rangle = \prod_l D_l(\alpha_n) \prod_{nm} S_{nm}(\xi_{nm}) |0\rangle. \quad (D13)$$

The expectation value  $\mathcal{Q}_n$  is given by Eq. (D5). When an even classical mode is dominant, e.g., mode 10, considered in the paper, the pair of modes  $\{n, m\}$ , where  $m = 10 - n$  experiences squeezing. In this case, squeezing in mode  $n = m = 5$  modifies the term  $\mathcal{N}_{5,5}$  while the two-mode squeezing changes  $\mathcal{A}_{1,9}, \mathcal{A}_{2,8}, \dots, \mathcal{A}_{9,1}$  when  $n \neq m$ . Thus, the off-diagonal terms of the anomalous correlation matrix contain information about the two-mode squeezed states. This result can be summarized in the following two equations:

$$\mathcal{N}_{nm}(t) = \frac{1}{2} \left( \alpha_n^* \alpha_m e^{-i(\omega_m - \omega_n)t} + \alpha_m^* \alpha_n e^{i(\omega_m - \omega_n)t} \right) + \sinh^2 |\xi_{nm}(t)| \delta_{nm} \delta_{n+m,10}, \quad (\text{D14})$$

$$\mathcal{A}_{nm}(t) = \frac{1}{2} \left( \alpha_n^* \alpha_m^* e^{i(\omega_m + \omega_n)t} + \alpha_m \alpha_n e^{-i(\omega_m + \omega_n)t} - \cos(\arg \xi_{nm}(t)) \sinh 2|\xi_{nm}(t)| \delta_{n+m,10} \right), \quad (\text{D15})$$

---

where, in the weakly driven regime [37] the steady state squeezing parameter is given by  $\xi_{nm}(t) = i\alpha_{10} e^{-i\omega_{10}t} A_{nm,10} T_*/\hbar$ . Note that this parameter is time dependent. Consequently, all three terms in the expression for  $\mathcal{A}_{nm}$  have the same frequency.

- [1] A. J. Leggett and A. Garg, *Physical Review Letters* **54**, 857 (1985).
- [2] J. M. Martinis, M. H. Devoret, and J. Clarke, *Physical Review Letters* **55**, 1543 (1985).
- [3] U. Vool and M. H. Devoret, *International Journal of Circuit Theory and Applications* **45**, 897 (2017), arxiv:1610.03438.
- [4] A. Blais, A. L. Grimsmo, S. M. Girvin, and A. Wallraff, *Reviews of Modern Physics* **93**, 025005 (2021).
- [5] S. J. Weber, G. O. Samach, D. Hover, S. Gustavsson, D. K. Kim, A. Melville, D. Rosenberg, A. P. Sears, F. Yan, J. L. Yoder, W. D. Oliver, and A. J. Kerman, *Physical Review Applied* **8**, 014004 (2017).
- [6] D. M. Tennant, X. Dai, A. J. Martinez, R. Trappen, D. Melanson, M. A. Yurtalan, Y. Tang, S. Bedkihal, R. Yang, S. Novikov, J. A. Grover, S. M. Disseler, J. I. Basham, R. Das, D. K. Kim, A. J. Melville, B. M. Niedzielski, S. J. Weber, J. L. Yoder, A. J. Kerman, E. Mozgunov, D. A. Lidar, and A. Lupascu, *npj Quantum Information* **8**, 85 (2022).
- [7] M. H. Devoret and R. J. Schoelkopf, *Science* **339**, 1169 (2013).
- [8] M. Kjaergaard, M. E. Schwartz, J. Braumüller, P. Krantz, J. I.-J. Wang, S. Gustavsson, and W. D. Oliver, *Annual Review of Condensed Matter Physics* **11**, 369 (2020).
- [9] D. Meiser and P. Meystre, *Physical Review A* **74**, 065801 (2006).
- [10] R. Kuzmin, N. Mehta, N. Grabon, R. Mencia, and V. E. Manucharyan, *npj Quantum Information* **5**, 20 (2019).
- [11] A. Smith, M. S. Kim, F. Pollmann, and J. Knolle, *npj Quantum Information* **5**, 1 (2019).
- [12] A. Burger, L. C. Kwek, and D. Poletti, *Entropy* **24**, 1766 (2022).
- [13] B. Fauseweh and J.-X. Zhu, *Quantum Information Processing* **20**, 138 (2021).
- [14] J. Braumüller, M. Marthaler, A. Schneider, A. Stehli, H. Rotzinger, M. Weides, and A. V. Ustinov, *Nature Communications* **8**, 779 (2017).
- [15] F. Arute, K. Arya, R. Babbush, D. Bacon, J. C. Bardin, R. Barends, A. Bengtsson, S. Boixo, M. Broughton, B. B. Buckley, D. A. Buell, B. Burkett, N. Bushnell, Y. Chen, Z. Chen, Y.-A. Chen, B. Chiaro, R. Collins, S. J. Cotton, W. Courtney, S. Demura, A. Derk, A. Dunsworth, D. Eppens, T. Eickl, C. Erickson, E. Farhi, A. Fowler, B. Foxen, C. Gidney, M. Giustina, R. Graff, J. A. Gross, S. Habegger, M. P. Harrigan, A. Ho, S. Hong, T. Huang, W. Huggins, L. B. Ioffe, S. V. Isakov, E. Jeffrey, Z. Jiang, C. Jones, D. Kafri, K. Kechedzhi, J. Kelly, S. Kim, P. V. Klimov, A. N. Korotkov, F. Kostritsa, D. Landhuis, P. Laptev, M. Lindmark, E. Lucero, M. Marthaler, O. Martin, J. M. Martinis, A. Maruszczyk, S. McArdle, J. R. McClean, T. McCourt, M. McEwen, A. Megrant, C. Mejuto-Zaera, X. Mi, M. Mohseni, W. Mruczkiewicz, J. Mutus, O. Naaman, M. Neeley, C. Neill, H. Neven, M. Newman, M. Y. Niu, T. E. O'Brien, E. Ostby, B. Pató, A. Petukhov, H. Putterman, C. Quintana, J.-M. Reiner, P. Roushan, N. C. Rubin, D. Sank, K. J. Satzinger, V. Smelyanskiy, D. Strain, K. J. Sung, P. Schmitteckert, M. Szalay, N. M. Tubman, A. Vainsencher, T. White, N. Vogt, Z. J. Yao, P. Yeh, A. Zalcman, and S. Zanker, *Observation of separated dynamics of charge and spin in the Fermi-Hubbard model* (2020), arxiv:2010.07965 [quant-ph].
- [16] Z. Yan, Y.-R. Zhang, M. Gong, Y. Wu, Y. Zheng, S. Li, C. Wang, F. Liang, J. Lin, Y. Xu, C. Guo, L. Sun, C.-Z. Peng, K. Xia, H. Deng, H. Rong, J. Q. You, F. Nori, H. Fan, X. Zhu, and J.-W. Pan, *Science* **364**, 753 (2019).
- [17] D. K. Weiss, W. DeGottardi, J. Koch, and D. G. Ferguson, *Physical Review Research* **3**, 033244 (2021), arxiv:2104.14377 [quant-ph].
- [18] R. Ma, B. Saxberg, C. Owens, N. Leung, Y. Lu, J. Simon, and D. I. Schuster, *Nature* **566**, 51 (2019).
- [19] N. Mehta, R. Kuzmin, C. Ciuti, and V. E. Manucharyan, *Nature* **613**, 650 (2023).
- [20] R. Kuzmin, R. Mencia, N. Grabon, N. Mehta, Y.-H. Lin, and V. E. Manucharyan, *Nature Physics* **15**, 930 (2019).
- [21] R. Kuzmin, N. Grabon, N. Mehta, A. Burshtein, M. Goldstein, M. Houzet, L. I. Glazman, and V. E. Manucharyan, *Physical Review Letters* **126**, 197701 (2021).
- [22] A. J. Kollár, M. Fitzpatrick, and A. A. Houck, *Nature* **571**, 45 (2019), arxiv:1802.09549 [cond-mat, physics:quant-ph].
- [23] A. L. Grimsmo and A. Blais, *npj Quantum Information* **3**, 1 (2017).
- [24] Z.-P. Cian, G. Zhu, S.-K. Chu, A. Seif, W. DeGottardi, L. Jiang, and M. Hafezi, *Physical Review Letters* **123**, 063602 (2019).
- [25] Y. Yanay, J. Braumüller, S. Gustavsson, W. D. Oliver, and C. Tahan, *npj Quantum Information* **6**, 58 (2020).
- [26] Y. Zhang, L. Yu, J.-Q. Liang, G. Chen, S. Jia, and F. Nori, *Scientific Reports* **4**, 4083 (2014).
- [27] L.-L. Zheng, K.-M. Li, X.-Y. Lü, and Y. Wu, *Physical Review A* **96**, 053809 (2017).
- [28] J. Jin, D. Rossini, R. Fazio, M. Leib, and M. J. Hartmann, *Physical Review Letters* **110**, 163605 (2013).
- [29] P. W. Anderson, *Science* **177**, 393 (1972), 1734697.
- [30] S. Hacohe-Gourgy and L. S. Martin, *Advances in Physics: X* **5**, 1813626 (2020).
- [31] T. Roy, A. M. Vadiraj, M. Chand, A. Ranadive, S. Kundu, M. P. Patankar, and R. Vijay, *Current Science* **109**, 2069 (2015), 24906706.
- [32] D. I. Schuster, A. A. Houck, J. A. Schreier, A. Wallraff, J. M. Gambetta, A. Blais, L. Frunzio, J. Majer, B. Johnson, M. H. Devoret, S. M. Girvin, and R. J. Schoelkopf, *Nature* **445**, 515 (2007).
- [33] D. F. Walls and G. J. Milburn, *Quantum Optics* (Springer, Berlin, Heidelberg, 1994).
- [34] S. M. Girvin, in *Quantum Machines: Measurement and Control of Engineered Quantum Systems: Lecture Notes of the Les Houches Summer School: Volume 96, July 2011*, edited by M. Devoret, B. Huard, R. Schoelkopf, and L. F. Cugliandolo (Oxford University Press, 2014) p. 0.
- [35] S. V. Lotkhov, R. Dolata, and M. Khabipov, *Applied Physics Letters* **115**, 192601 (2019).
- [36] J. A. Grover, J. I. Basham, A. Marakov, S. M. Disseler, R. T. Hinkey, M. Khalil, Z. A. Stegen, T. Chamberlin, W. DeGottardi, D. J. Clarke, J. R. Medford, J. D. Strand, M. J. A. Stoutimore, S. Novikov, D. G. Ferguson, D. Lidar, K. M. Zick, and A. J. Przybysz, *PRX Quantum*

- 1, 020314 (2020).
- [37] H. Seifoory, S. Doustre, M. M. Dignam, and J. E. Sipe, The properties of squeezed optical states created in lossy cavities (2016), arxiv:1608.05005 [physics, physics:quant-ph].
- [38] M. Gluza, T. Schweigler, B. Rauer, C. Krumnow, J. Schmiedmayer, and J. Eisert, *Communications Physics* **3**, 1 (2020).
- [39] M. Tajik, M. Gluza, N. Sebe, P. Schüttelkopf, F. Cataldini, J. Sabino, F. Møller, S.-C. Ji, S. Erne, G. Guarneri, S. Sotiriadis, J. Eisert, and J. Schmiedmayer, *Proceedings of the National Academy of Sciences* **120**, e2301287120 (2023).
- [40] M. Tajik, I. Kukuljan, S. Sotiriadis, B. Rauer, T. Schweigler, F. Cataldini, J. Sabino, F. Møller, P. Schüttelkopf, S.-C. Ji, D. Sels, E. Demler, and J. Schmiedmayer, *Nature Physics* **19**, 1022 (2023).
- [41] A. Roy, D. Schuricht, J. Hauschild, F. Pollmann, and H. Saleur, *Nuclear Physics B* **968**, 115445 (2021), arxiv:2007.06874 [cond-mat, physics:hep-lat, physics:nlin, physics:quant-ph].